Exploring surface source contributions to ocean ambient noise interferometry with airgun shots

John Ragland[a] and Shima Abadi[b]

Electrical and Computer Engineering, University of Washington, Seattle, Washington 98195, USA

ABSTRACT:

A seismic reflection survey conducted directly over two bottom-mounted hydrophones in the north-east Pacific Ocean is used to explore how surface source locations affect ambient noise interferometry for the two hydrophones. The airgun shots are used as an approximation of an impulsive sound source at a discrete location, which allows us to investigate spatial contributions to the cross correlation between the two hydrophones. Simulated and experimental results are presented. The contributions to the cross correlations are explained by different reflections off the surface or bottom of the ocean, and a discussion about what can and cannot be inferred about the emergence to the Green's function is presented. © *2022 Author(s). All article content, except where otherwise noted, is licensed under a Creative Commons Attribution (CC BY) license (http://creativecommons.org/licenses/by/4.0/).*
https://doi.org/10.1121/10.0015231

I. INTRODUCTION

The goal of ambient noise interferometry is to use ambient sound to infer information about acoustic propagation without any prior knowledge of the ambient sound statistics or sound source distribution. In free space for an isotropic sound source distribution that is uncorrelated in space and time, the derivative of the correlation between two sensors will be the time domain Green's function between the two sensors (Roux *et al.*, 2005; Snieder, 2004; Weaver and Lobkis, 2004). Unfortunately, sound sources in the ocean are neither uniformly distributed or uncorrelated in space and time. Knowing how individual sound source locations contribute to the correlation between two sensors is important for understanding how the convergence to the time domain Green's function will be affected for arbitrary sound source distributions or propagating environments. In this work, a seismic reflection survey that was conducted directly over two bottom-mounted hydrophones in the north-east Pacific Ocean will be utilized to experimentally measure the cross correlation sensitivity kernel (Skarsoulis and Cornuelle, 2020) and characterize the spatial source contributions to the correlation between the sensors.

For a homogeneous medium with attenuation and an isotropic noise source distribution, the Green's function can be recovered from the cross correlation between two sensors (Roux *et al.*, 2005). For a Pekeris oceanic waveguide, the Green's function can also be estimated for a uniform surface distribution of sound sources (Sabra *et al.*, 2005). For this distribution, the cross correlation function between two sensors converges to an amplitude shaded estimate of the Green's function. Sources located along acoustic ray paths that connect the two sensors contribute to the empirical Green's function estimate and therefore constructively add together when cross correlations are averaged together (Godin, 2009).

Ambient noise interferometry in the ocean has been experimentally demonstrated for various propagating environments and sound sources. It has also been successfully used for passive acoustic tomography. In Roux and Kuperman (2004), the frequency band dominated by shipping noise was used to measure the empirical Green's function. In Fried *et al.* (2008), the frequency band dominated by croaker fish vocalizations is utilized for ambient noise interferometry, and empirical Green's functions matched simulated results well. In Brooks and Gerstoft (2009), a tropical storm is utilized for ambient noise interferometry. Godin (2009) use vertical line arrays in the north Pacific to estimate the empirical Green's function and successfully infer information about the sound speed structure. Utilizing data collected off the coast of Florida, empirical Green's functions were successfully recovered and were used for inferring modal dispersion, flow velocity estimation, estimating bottom properties, and time reversal (Brown *et al.*, 2014; Brown *et al.*, 2016; Godin *et al.*, 2014; Godin *et al.*, 2017; Tan *et al.*, 2019; Zang *et al.*, 2015). Utilizing deep sound propagating channels and ice breaking events, the temperature of the deep ocean has also been measured using ambient noise interferometry (Evers *et al.*, 2017; Woolfe and Sabra, 2015; Woolfe *et al.*, 2015). Dispersion curves for the first three modes have been passively measured for a highly dynamic, shallow ocean, using a horizontal line array off the coast of New Jersey (Tan and Godin, 2021; Tan *et al.*, 2020). Ambient noise interferometry has also been demonstrated for bottom-mounted hydrophones in the deep ocean with strong contributions from multi-path arrivals (Ragland *et al.*, 2022a).

[a] Electronic mail: jhrag@uw.edu
[b] Also at: Division of Engineering and Mathematics, University of Washington, Bothell, WA 98011, USA.

The effects of anisotropic noise source distributions have been explored by several works. Godin (2009) demonstrates that if the noise source distribution varies gradually in space, travel times can be accurately estimated using ambient noise interferometry. Weaver *et al.* (2009) derive a correction factor for estimated arrival times given a directionality of ambient sound. Buckingham (2011) uses the ambient noise model proposed by Cron and Sherman (1962, 1965) to study the model's effects on the vertical and horizontal wave coherence between two sensors. This model consists of a uniform distribution of sound sources at the surface of the ocean with no bottom. Walker and Buckingham (2012) expand this work to additionally include a non-isotropic horizontal distribution of noise sources. Walker and Buckingham (2012) find that, given a non-isotropic distribution of noise sources, horizontal coherence between two sensors still contains information about the Green's function between the two sensors, but that the derivative in time of the coherence does not explicitly equal the Green's function between the two sensors. Walker (2012) investigates the effects of anisotropic noise on how wave coherence constructively and destructively interferes. Specifically, Walker (2012) show that even for heavily directional ambient sound, only sound that travels through both sensors contributes significant energy to the coherence between the two sensors.

Recently, numerical methods have been used to explore the effects of complex refracting environments on ambient noise interferometry (Skarsoulis and Cornuelle, 2019, 2020). A method is developed to numerically simulate the cross correlation between two sensors, given a distribution of sound sources (Skarsoulis and Cornuelle, 2019). They discover that there are sound speed profiles and hydrophone geometries that do not result in the convergence of the cross correlation to the empirical Green's function, given a uniform surface distribution of sound sources. This is because, for certain propagation environments and hydrophone geometries, acoustic ray paths that connect both hydrophones do not intersect with the surface. Skarsoulis and Cornuelle (2020) develop a metric called the cross correlation sensitivity kernel that evaluates how a source located at a specific point in space affects the cross correlation at specific delay times. In Roux *et al.* (2013), sensitivity kernels are experimentally measured and compared to theoretical results for acoustic scattering in the ultrasonic band. In recent work, Cornuelle and Skarsoulis (2022) explore the sensitivity of empirical Green's function peak times to changes in water sound speed.

In this paper, a seismic reflection survey will be used to experimentally measure the cross correlation sensitivity kernel and characterize the spatial contribution of sound sources on the cross correlation function. Two hydrophones that are part of the Ocean Observatories Initiative (OOI), separated by 3.19 km, and are bottom mounted at a depth of 1500 m will be used for the analysis. The patterns that are observed in the experimental and simulated cross correlation sensitivity kernels are then explained and related to different

reflections off the surface or bottom of the ocean using the method of images. Last, what can and cannot be learned from the cross correlation sensitivity kernel will be discussed.

In Sec. II, information about the experiment and details about the data processing are presented. In Sec. III, a review of the sensitivity kernel is presented. Section IV A presents the simulated results and Sec. IV B presents the experimentally measured cross correlation sensitivity kernel. An explanation for these results is presented in Sec. IV C. Last, a discussion and conclusion of the findings are presented in Sec. V B.

II. EXPERIMENTAL SETUP

In this section, the hydrophone and airgun experiment geometries will be described as well as the data processing that was completed for the subsequent analysis.

We are using two hydrophones that are 270 km off the Oregon coast and are part of the OOI network. Ambient noise interferometry has previously been demonstrated for these two hydrophones (Ragland *et al.*, 2022a). The two hydrophones that we are using are the *Central Caldera* (NSF Ocean Observatories Initiative Data Portal, 2022a) and *Eastern Caldera* (NSF Ocean Observatories Initiative Data Portal, 2022b) hydrophones. These hydrophones are separated by 3.186 km, bottom mounted at depths of 1527 m and 1518 m, respectively, and are calibrated to 0.001995 V/Pa and 0.00195 V/Pa, respectively between 2–90 Hz. The sampling rate is 200 Hz. Acoustic data are downloaded using the python package OOIPy (Schwock *et al.*, 2022). The seismic reflection survey that we are utilizing is the MGL1905 cruise conducted between July 9, 2019, and August 14, 2019 (Langseth, 2022). The location of the vessel and experiment logs are publicly available. The sea state during experimental lines was generally around 4, with a few experimental lines reporting a sea state of 5, as defined by World Meteorological Organization (2015). This seismic reflection survey included 36 airguns that are towed behind the research vessel at a depth of 12 m and 230 m behind the research vessel. For this analysis, the assumption is that the airgun array is a point source. Spectrograms of airgun shots recorded by OOI hydrophones are reported in Ragland *et al.* (2022b).

For the subsequent analysis in Sec. IV, a single noise cross correlation function (NCCF) needs to be associated with a point in space where the airgun was fired. In this paper, the term NCCF will be used to describe the physically processed data that include a finite averaging time and any other data processing. The term cross correlation will refer to the expectation of the correlation between two sensors.

During a line of the experiment, the time between airgun shots is approximately 18 s, and the average speed of the vessel is approximately 4.2 knots. The location of the vessel and the NCCFs are averaged to the same time grid with an averaging time of 2 min. This means that each calculated NCCF contains approximately 6 airgun shots, and the distance covered by the research vessel is approximately

270 m. For the sake of this analysis, the distance traveled by the research vessel during the 2 min averaging time and the length of the airgun lines behind the research vessel are considered to be negligible. Data are only kept during lines of the airgun experiment and when acoustic data from both hydrophones exist. Additionally, data from the last four lines of the experiment are discarded because of the non-symmetric path of the ship and higher source levels of the airgun. This resulted in 304 h of acoustic data. Figure 1 shows a map of the 2 min average airgun locations that have associated NCCFs. The two hydrophones are labeled (*Eastern Caldera* and *Central Caldera*) as well as the location of the ocean profiler data used for analysis (*Axial Base*).

To calculate the NCCFs, acoustic data are downloaded from OOI using the python package OOIPy (Schwock *et al.*, 2022), separated into 30 s segments and filtered between 1 and 90 Hz using a 4th order, zero-phase, Butterworth filter. The 30 s data segments from each hydrophone are then cross correlated and averaged together for 2 min.

The latitude and longitude coordinates of the research vessel are transformed into a Cartesian coordinate system in kilometers, where the origin is the midpoint between the two hydrophones and the x axis is the axis connecting the hydrophones. Therefore, the coordinate of the *Central Caldera* hydrophone is $(-1.59, 0)$ km and the coordinate of the *Eastern Caldera* hydrophone is $(1.59, 0)$ km. The latitude and longitude coordinates are transformed by calculating the range from the hydrophone midpoint and the bearing from the hydrophone midpoint assuming a spherical earth and transforming these polar coordinates to Cartesian coordinates.
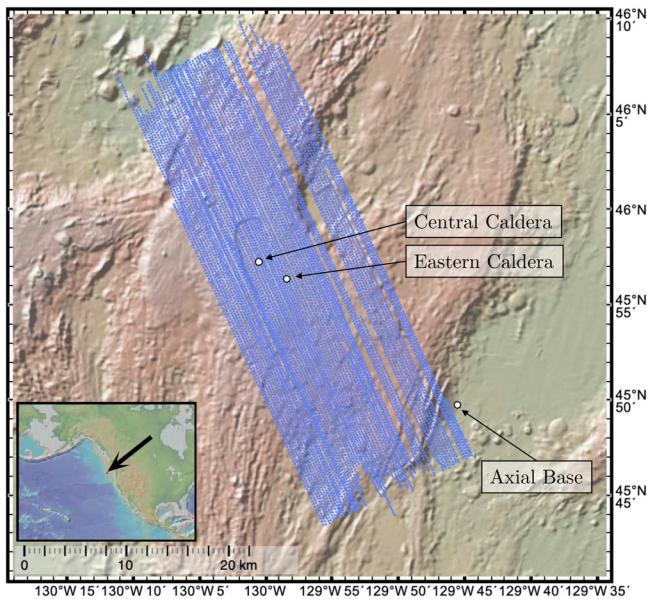

FIG. 1. (Color online) Map of the 2 min average airgun locations that have associated NCCFs and the locations of the two hydrophones that are used to calculate the NCCFs. The hydrophone on the left is the *Central Caldera* hydrophone and the hydrophone on the right is the *Eastern Caldera* hydrophone.

III. THEORETICAL BACKGROUND

The cross correlation sensitivity kernel (Skarsoulis and Cornuelle, 2020) is a function of both space and time and is a metric that evaluates what locations contribute to a cross correlation between the two sensors for different delay times. The cross correlation sensitivity kernel is defined in Eq. (1) and Eq. (2), where $K(\mathbf{x}, \tau; \mathbf{x_1}, \mathbf{x_2})$ is the cross correlation sensitivity kernel, $S(\mathbf{x})$ is the source distribution density, $H(\omega)$ is the receiver response, $\mathbf{x_1}$ and $\mathbf{x_2}$ are the location of the two sensors, and $G(\omega; \mathbf{x_1}|\mathbf{x})$ is the Green's function at location $\mathbf{x_1}$ due to a source located at $\mathbf{x}$,

$$C_{1,2}(\tau) = \iiint_V K_\tau(\mathbf{x}, \tau; \mathbf{x_1}, \mathbf{x_2}) \cdot S(\mathbf{x}) dV(\mathbf{x}), \qquad (1)$$

$$K_\tau(\mathbf{x}, \tau; \mathbf{x_1}, \mathbf{x_2}) = \frac{1}{2\pi} \int_{-\infty}^{\infty} |H(\omega)|^2 G(\omega; \mathbf{x_1}|\mathbf{x})$$
$$\times G^*(\omega; \mathbf{x_2}|\mathbf{x}) e^{j\omega\tau} d\omega. \qquad (2)$$

From inspection, the Fourier transform of the cross correlation sensitivity kernel can be written as

$$K_\omega(\mathbf{x}, \omega; \mathbf{x_1}, \mathbf{x_2}) = |H(\omega)|^2 G(\omega; \mathbf{x_1}|\mathbf{x}) G^*(\omega; \mathbf{x_2}|\mathbf{x}). \quad (3)$$

Looking at Eq. (3), one can see that the cross correlation sensitivity kernel is composed of the frequency response of the sensors and the cross correlation in time of the Green's functions between $\mathbf{x_1}$ and $\mathbf{x}$, and the Green's function between $\mathbf{x_2}$ and $\mathbf{x}$. Therefore, given a uniform sensor response, the sensitivity kernel is the cross correlation between two sensors for a single, impulsive point source located at $\mathbf{x}$. Although the airgun is designed to have a specific beam pattern at specific frequencies, the broadband beam pattern of the airgun shots is relatively flat relative to the dB scales we are measuring in this work (Douglass and Abadi). For this analysis, we are ignoring airgun shot variations. Additionally, given the airgun shot period of 18 s and the hydrophone separation of 3.19 km (corresponding to a direct path of 2.1 s), a single NCCF sample results in the same airgun shots being recorded by both hydrophones. We therefore can assume that the airgun source is stationary. Given these assumptions, at the frequencies we are studying, an airgun shot is a good approximation of an impulse function. This allows us to experimentally measure the cross correlation sensitivity kernel. An NCCF that is formed by averaging over all experiment lines would be the same as integrating Eq. (1) over the spatial region defined in Fig. 1. Since this source distribution is not isotropic, it is not necessarily guaranteed to converge to an empirical Green's function.

IV. RESULTS

In this section, the cross correlation sensitivity kernel is simulated for the given hydrophone geometry and compared to measured results that utilize airgun shots to experimentally measure the cross correlation sensitivity kernel.

J. Acoust. Soc. Am. **152** (5), November 2022

John Ragland and Shima Abadi   3071

The patterns that are observed in the surface slices of the cross correlation sensitivity kernel are explained using geometry.

A. Numerical results

The cross correlation sensitivity kernel in Eq. (2) can be numerically simulated using any wave-theoretic method to solve for the two Green's functions. For this analysis, the Green's functions are calculated using normal mode propagation and are solved using Kraken (Porter, 1992). The oceanic waveguide is assumed to be range independent with a depth of 1523 m. The two hydrophones are placed at a depth of 1522 m. The sound speed profile used for simulation is measured by the *Axial Base* ocean profiler from OOI, located approximately 20 km from the two hydrophones (see Fig. 1). A single, average sound speed profile that was measured between July 15, 2019, and August 15, 2019, will be used for all analysis. The ocean surface was assumed to be a pressure release and the ocean bottom was assumed to be an acousto-elastic half space with a bottom sound speed of 1749 m/s and a density of 1.88 g/cm^3. The time domain Green's function (TDGF) is sampled for 30 s at a sampling rate of 200 Hz (number of points: 6000, frequency bin width: 0.033 Hz, frequency step of 0.33 Hz). Figure 2(a) shows the sound speed profile used for simulation and Fig. 2(b) shows the simulated time domain Green's function between the two hydrophones using normal mode propagation. The Green's function is simulated in the frequency band 0–100 Hz for 0–30 s with a sampling rate of 200 Hz. The Green's function is then multiplied in the frequency domain by the response of the digital filter described in Sec. II. All subsequent Green's functions that are simulated in the following analysis are calculated using this same method. Figure 2(c) shows the first 4 eigen rays (simulated with BELLHOP (Siderius and Porter, 2008). At this frequency, ray-theoretic methods are not an accurate solution to the wave equation, but they provide intuition into how the waves are propagating and will provide helpful context for further discussions. The peak in Fig. 2(b) at 2.1 s is due to the direct path, the peak at 2.9 s is due to the ray path that bounces off the surface once, and the peak at 4.6 s is due to the ray path that bounces off the surface twice and the bottom once.

Figure 3 shows the horizontal slice at a depth of 12 m of the simulated cross correlation sensitivity kernel as defined in Eq. (2) for several delay times (plotted in blue). The slice is simulated at a depth of 12 m because this is the depth of the airguns. The absolute values of the amplitudes are plotted in dB relative to the maximum value at $\tau = 0$ s. The solid and dashed lines appearing in this figure are slices of hyperboloids that are explained in Sec. IV C. In this analysis, we present the positive delay times which characterizes acoustic propagation from *Eastern Caldera* to *Central Caldera*. Negative delay times are not shown but are symmetric to positive delay times along the y axis.

In Fig. 3(a), the cross correlation sensitivity kernel is shown for the delay time of $\tau = 0.1$ s ($\tau = 0.1$ s is chosen instead of 0 s for numerical issues in plotting the hyperboloid slices). The vertical line at $x = 0$ km represents sources that are equidistant from each hydrophone and therefore contribute to the cross correlation at a delay time of $\tau = 0$. The other vertical lines are caused by reflections off the bottom or surface of the ocean. In Fig. 3(b), the cross correlation sensitivity kernel is shown for delay time $\tau = 1.8$ s. In Fig. 3(c), the cross correlation sensitivity kernel is shown for delay time $\tau = 2.6$ s. For both $\tau = 1.8$ s and $\tau = 2.6$ s, there are no arrivals in the TDGF between the two hydrophones. This means that sources that contribute to this delay time will average out of the cross correlation, given a uniform noise source distribution. Figure 3(d) shows the cross correlation sensitivity kernel for delay time $\tau = 2.965$ s. This is the arrival time of the surface reflection peak as seen in Fig. 2(b). In the frequency band where ray-theoretic formulations are valid solutions to the wave equations, sources that contribute to arrival times in the cross correlation are located along rays that pass through the two sensors (Godin,
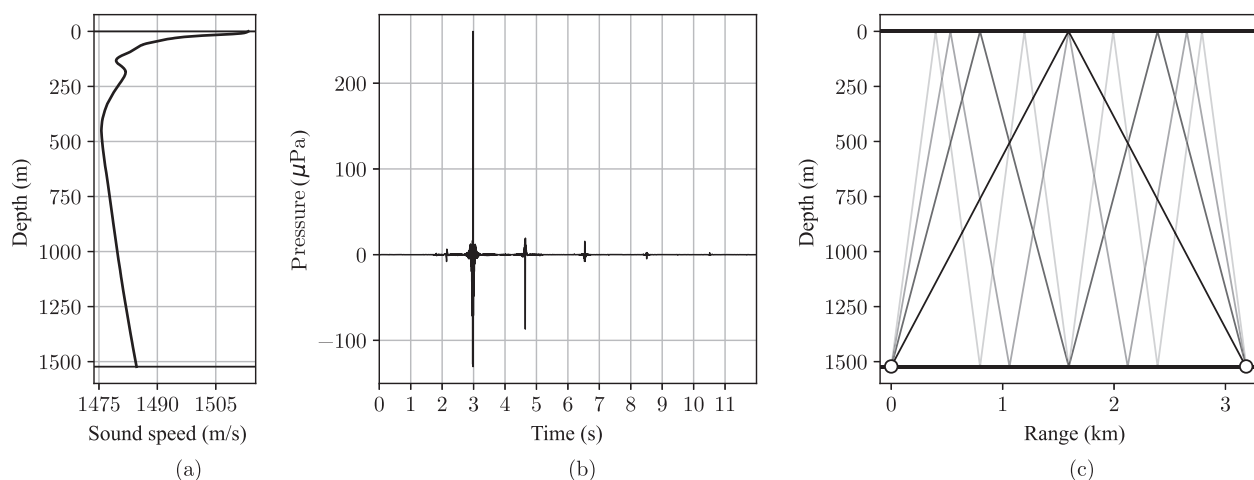

FIG. 2. (a) Average sound speed profile measured by the *Axial Base* ocean profiler from OOI during the airgun experiment. (b) The simulated, band limited, time domain Green's function between the two hydrophones. This was simulated with normal modes and using the Kraken code to solve for the modes (Porter, 1992) (c) The first four eigen rays between the two hydrophones solved with BELLHOP (Siderius and Porter, 2008).
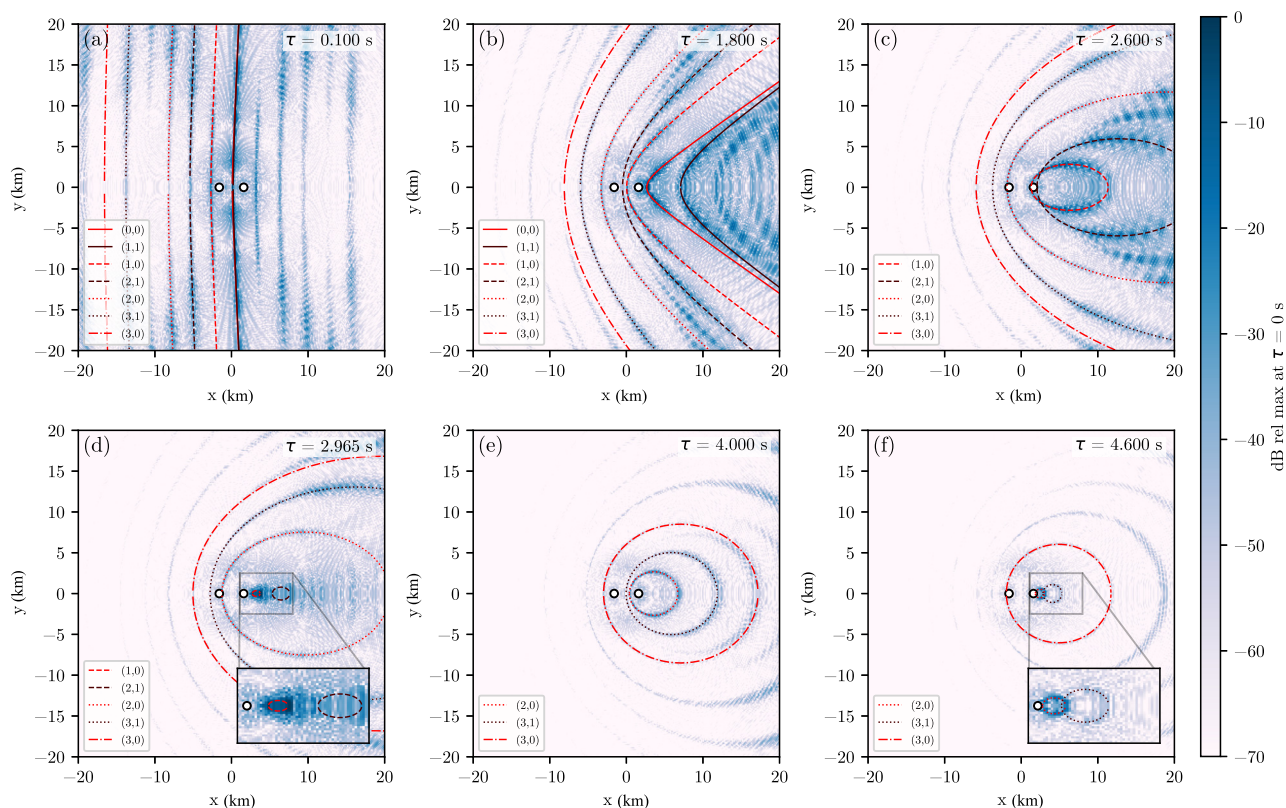
FIG. 3. (Color online) (a)–(f) Horizontal slice of the simulated cross correlation sensitivity kernel at a depth of 12 m for different delay times. The cross correlation sensitivity kernel is plotted in blue. The red lines are slices of hyperboloids that explain the different patterns as described in Sec. IV C.

2009). The ray path associated with an arrival at $\tau = 2.96$ s is the darkest ray path plotted in Fig. 2(c) and reflects off the surface of the ocean once. Sources along this ray path extension that are located on the surface of the ocean would be expected to be at discrete ranges separated by the distance of the two hydrophones. Figure 3(e) shows the cross correlation sensitivity kernel for delay time $\tau = 4.0$ s. This delay time, like the delay times of 1.8 s and 2.6 s, does not correspond to an arrival time in the TDGF. Figure 3(f) shows the cross correlation sensitivity kernel for the delay time $\tau = 4.60$, which is just before the second arrival in the TDGF. This arrival time is associated with the ray path that reflects off the surface twice and the bottom once. The hot spots visible in Fig. 3(f) correspond with the intersections of this ray extension with the surface of the ocean. Further investigation into the curves seen in the cross correlation sensitivity kernel for different delay times will be presented in Sec. IV C.

B. Experimental results

Figure 4 shows the experimentally measured cross correlation sensitivity kernels for different delay times (plotted in blue). To reduce noise, the root mean squared amplitude of the cross correlation is presented for a window length of 0.02 s centered around the reported delay time. The solid and dashed red lines are hyperboloid slices that are explained in Sec. IV C. The simulated and measured results are in good agreement. The measured results

have more attenuation due to surface or bottom reflections. This discrepancy is likely due to the environmental parameters chosen for the simulated environment not perfectly matching the physical bottom properties of the ocean. Additionally, since the research vessel is moving during the experiment, the Doppler effect degrades coherence for non–end-fire samples of the cross correlation sensitivity kernel. In the end-fire direction, loss of coherence due to Doppler shift is zero since the radial ship velocity for the two hydrophones is identical. Negative delay times are not shown but are symmetric to positive delay times along the y axis. An animation for all delay times between 0 and 7 s is provided for the simulated and experimentally measured cross correlation sensitivity kernels (See supplementary material for photograph of the device).[1]

C. Explaining patterns in the cross correlation sensitivity kernel

For the case of free space propagation in a homogeneous medium, different delay times in the cross correlation are caused by sources located on the surface of a hyperboloid (Roux *et al.*, 2005). The hyperboloid is defined by a constant difference in range between the two sensors and a given point in space. For the case of a homogeneous medium, this constant difference in range corresponds to a constant difference in propagation time. The two sensors are located in the foci of the hyperboloid. Different delay times correspond to how "open" the hyperbola is, where a delay
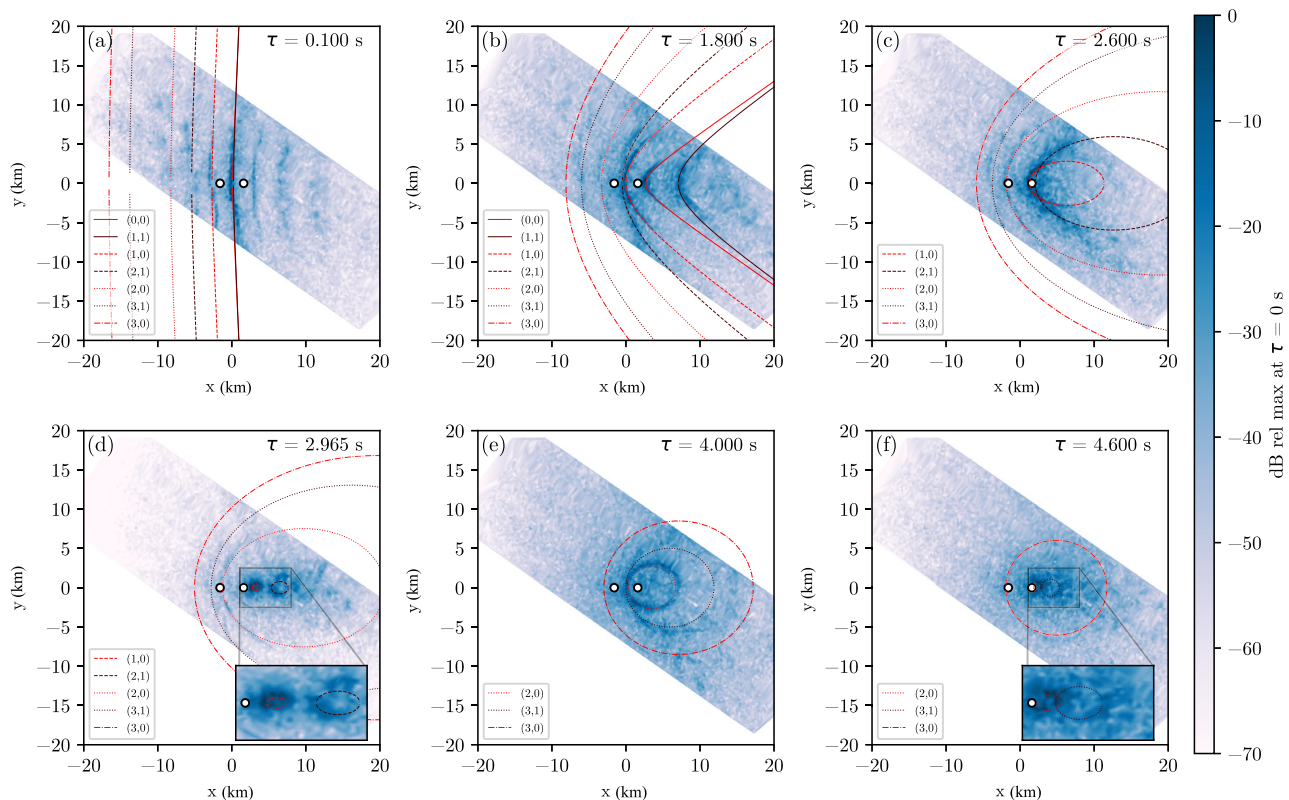
FIG. 4. (Color online) (a)–(f) Horizontal slice of the experimentally measured cross correlation sensitivity kernel using airgun shots. The NCCFs are plotted for different delay times and airgun locations in blue. The red lines are slices of hyperboloids that explain the different patterns as described in Sec. IV C.

time corresponding to 0 s corresponds to a constant line in the broadside of the two sensors. This represents sources that are equidistant from both sensors. A delay time equal to D/c, where D is the distance between the hydrophones and c is the speed of wave propagation in the medium, corresponds to a line pointing in the end-fire direction of the sensors. This has also previously been utilized in time difference of arrival beamforming, where an approximation of the bearing of a source is a function of delay time and is also derived by utilizing hyperbolas (Carter, 1981).

As can be seen in Fig. 2(c), due to the small separation of the hydrophones, refraction does not affect the ray paths significantly. Therefore, a constant sound speed equal to the average sound speed of the water column can be used to approximate acoustic wave propagation in this environment. The boundary conditions of the oceanic waveguide can be accounted for by using the method of images. Given these assumptions, equations for hyperboloids that correspond to different pairs of hydrophones or hydrophone images can be derived. The method of images has previously been used to prove that a uniform distribution of surface sources results in the convergence of the cross correlation to an amplitude shaded Green's function for a Pekeris waveguide (Sabra *et al.*, 2005).

The source locations that contribute to the cross correlation for our (simplified) environment, therefore lie on the surfaces of hyperboloids formed by different image orders of sensor 1 and sensor 2. The sources that contribute to the cross correlation along the plane defined by a constant depth

of 12 m can therefore be explained by a horizontal slice of these hyperboloids at a depth of 12 m.

Figure 5 gives a schematic of this problem formulation. Different image orders are referenced numerically where 0 indicates the physical hydrophones and 1 would indicate the first image. A specific hyperboloid is referenced using the image index of each sensor that is used to define the foci of a hyperboloid. For instance, the light red (dashed line) hyperbola shown in Fig. 5 is referenced by the index pair (0,0). This means that
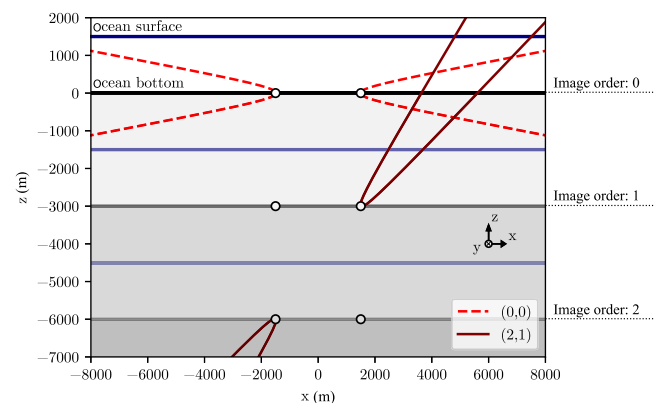

FIG. 5. (Color online) Schematic of the hyperboloids that are formed using the method of images. Each hyperboloid is indexed by the image order of the two hydrophones that are used to define the hyperboloid. The hydrophones are located in the foci of the hyperbola, but appear to be located on the hyperbola due to the scale.

3074   J. Acoust. Soc. Am. **152** (5), November 2022

John Ragland and Shima Abadi

the foci of the hyperboloid are located at the physical location of sensor 1 and the physical location of sensor 2. The dark red (solid line) hyperbola shown in Fig. 5 is referenced by the index pair (2,1). This means that the foci of the hyperboloid are located at the second image order location for sensor 1 and the first image order location for sensor 2.

The plotted lines in Figs. 3 and 4 are the hyperboloid slices for some of the relevant hydrophone image pairs. Hyperboloid slices with the same dash pattern correspond to hydrophone image pairs that have parallel axes. For instance, the solid lines correspond to (0,0) and (1,1). The color of the lines corresponds to the image pair of the sensor on the right. For instance, the light red lines correspond to hyperboloid slices that correspond to the physical sensor on the right, while the brown lines correspond to hyperboloid slices that correspond to the first image of the hydrophone on the right. Not every hyperboloid slice that shows up in the cross correlation sensitivity kernel is plotted. For instance, in Fig. 3(b), the curves in the cross correlation sensitivity kernel that are to the right of the two solid lines correspond to image pairs of (2,2) and (3,3). In Figs. 3 and 4, it can clearly be seen that the patterns seen in the cross correlation sensitivity kernel have good agreement with the geometrically derived hyperboloid slices. The concentric circle patterns (most clearly seen for delay times greater that $\tau = 2.6$ s) are explained by hyperboloid slices formed by hydrophone image pairs that have parallel axes. The circles get smaller for greater delay times because of the hyperboloids closing. The analytical expressions for all plotted hydrophones are provided in the Appendix.

V. DISCUSSION AND CONCLUSION

In the following sections, a discussion on why the cross correlation sensitivity kernel has non–end-fire contributions will be discussed, and the results will be summarized.

A. Cross-correlation sensitivity kernel and Green's function emergence

In Figs. 3 and 4, energy that is not in the end-fire direction and more specifically, not along ray path extensions that connect the two hydrophones is clearly present. Off end-fire energy is even present during delay times that correspond to arrival times in the time domain Green's function between the two sensors [see Figs. 4(d) or 4(f)]. As explained in Sec. IV C, patterns in the cross correlation sensitivity kernel are caused by hyperboloid slices created by different surface or bottom reflections, but why do we see energy in the cross correlation sensitivity kernel that does not contribute to the TDGF?

The cross correlation sensitivity kernel represents the locations in space that contribute energy to different delay times between two sensors. As mentioned in Sec. III, the cross correlation sensitivity kernel can be interpreted as the cross correlation between two sensors located at $\mathbf{x_1}$ and $\mathbf{x_2}$ for a single, impulsive sound source located at $\mathbf{x}$. Since the cross correlation sensitivity kernel considers a single point

in space, the amplitude of the cross correlation sensitivity kernel does not include information about how sources will constructively or destructively interfere when integrated over a given source distribution. This means that the amplitude of the cross correlation sensitivity kernel will not be larger along ray path extensions, or in the end-fire direction at arrival times. This explains why we see energy in the cross correlation sensitivity kernel for all delay times, and why at arrival times, the cross correlation sensitivity kernel contains energy from other hydrophone image pairs. The amplitude of the cross correlation sensitivity kernel, therefore, does not characterize which sources contribute to or degrade in the emergence of the time domain Green's function between the two hydrophones. The effects of a single impulsive source and a distribution of sound sources on the amplitude of the cross correlation is demonstrated well in Figs. 4 and 5 in Skarsoulis and Cornuelle (2019).

The cross correlation sensitivity kernel is a useful tool for providing intuition about how a specific source location will affect the cross correlation between the two sensors. However, the amplitude of the cross correlation sensitivity kernel should not be confused as containing information about how a cross correlation will converge to the empirical Green's function for an arbitrary source distribution. The constructive and destructive interference is determined by the volume integral in Eq. (1).

B. Conclusion

In conclusion, the cross correlation sensitivity kernel for two bottom-mounted hydrophones is simulated and experimentally measured using a seismic reflection survey as data of opportunity. Given the geometry and propagating environment of the two hydrophones, strong multi-path arrivals are present in the Green's function between the two hydrophones. This significantly affects the patterns that are seen in the horizontal slices of the cross correlation sensitivity kernel. Using a model of a constant sound speed throughout the water column, the shapes in the cross correlation sensitivity kernel can be geometrically explained by using the method of images and taking horizontal slices of the hyperboloids that are formed by different hydrophone image combinations for a specific delay time. Last, this specific hydrophone geometry and propagating environment illuminates how the cross correlation sensitivity kernel does not exclusively contain information about how a specific source location will contribute to the empirical Green's function between the two hydrophones.

ACKNOWLEDGMENTS

APPENDIX

The equations for hyperboloid slices corresponding to every image contribution that is plotted in Figs. 3 and 4 are

TABLE I. Hyperboloid index pairs as defined in Sec. IV C and the corresponding equation numbers.

Hyperboloid indexes	Equation number
(0,0)	(A1)
(1,0)	(A2)
(2,0)	(A3)
(3,0)	(A4)
(1,1)	(A5)
(2,1)	(A6)
(3,1)	(A7)

given below. In the following equations, L is half the distance between the hydrophones, H is the depth of the water, z_s is the depth of the horizontal slice, C is the speed of sound, τ is delay time, and x and y are Cartesian coordinates. For the curves shown in Figs. 3 and 4, the values of $L = 3.186/2$ km, $H = 1523$ m, $z_s = 12$ m, and $C = 1480.33$ m/s are used. The hydrophones are assumed to be directly on the ocean bottom, instead of at 1522 m. Table I gives the hyperboloid index pair as defined in Sec. IV C and the corresponding equation number,

$$\left(\frac{4x^2}{C^2\tau^2} - 1\right)\left(L^2 - \frac{C^2\tau^2}{4}\right) - y^2 - (H - z_s)^2 = 0, \quad (A1)$$

$$\left(\frac{4\left(\frac{Lx}{\sqrt{H^2+L^2}} + \frac{H(2H - z_s)}{\sqrt{H^2+L^2}}\right)^2}{C^2\tau^2} - 1\right)$$
$$\times \left(-\frac{C^2\tau^2}{4} + H^2 + L^2\right)$$
$$- \left(\frac{Hx}{\sqrt{H^2+L^2}} - \frac{L(2H - z_s)}{\sqrt{H^2+L^2}}\right)^2 - y^2 = 0, \quad (A2)$$

$$\left(\frac{4\left(\frac{Lx}{\sqrt{4H^2+L^2}} + \frac{2H(3H - z_s)}{\sqrt{4H^2+L^2}}\right)^2}{C^2\tau^2} - 1\right)$$
$$\times \left(-\frac{C^2\tau^2}{4} + 4H^2 + L^2\right)$$
$$- \left(\frac{2Hx}{\sqrt{4H^2+L^2}} - \frac{L(3H - z_s)}{\sqrt{4H^2+L^2}}\right)^2 - y^2 = 0, \quad (A3)$$

$$\left(\frac{4\left(\frac{Lx}{\sqrt{9H^2+L^2}} + \frac{3H(4H - z_s)}{\sqrt{9H^2+L^2}}\right)^2}{C^2\tau^2} - 1\right)$$
$$\times \left(-\frac{C^2\tau^2}{4} + 9H^2 + L^2\right)$$
$$- \left(\frac{3Hx}{\sqrt{9H^2+L^2}} - \frac{L(4H - z_s)}{\sqrt{9H^2+L^2}}\right)^2 - y^2 = 0, \quad (A4)$$

$$\left(\frac{4x^2}{C^2\tau^2} - 1\right)\left(L^2 - \frac{C^2\tau^2}{4}\right) - (3H - z_s)^2 - y^2 = 0, \quad (A5)$$

$$\left(\frac{4\left(\frac{Lx}{\sqrt{H^2+L^2}} + \frac{H(4H - z_s)}{\sqrt{H^2+L^2}}\right)^2}{C^2\tau^2} - 1\right)$$
$$\times \left(-\frac{C^2\tau^2}{4} + H^2 + L^2\right)$$
$$- \left(\frac{Hx}{\sqrt{H^2+L^2}} - \frac{L(4H - z_s)}{\sqrt{H^2+L^2}}\right)^2 - y^2 = 0, \quad (A6)$$

$$\left(\frac{4\left(\frac{Lx}{\sqrt{4H^2+L^2}} + \frac{2H(5H - z_s)}{\sqrt{4H^2+L^2}}\right)^2}{C^2\tau^2} - 1\right)$$
$$\times \left(-\frac{C^2\tau^2}{4} + 4H^2 + L^2\right)$$
$$- \left(\frac{2Hx}{\sqrt{4H^2+L^2}} - \frac{L(5H - z_s)}{\sqrt{4H^2+L^2}}\right)^2 - y^2 = 0. \quad (A7)$$

[1]See supplementary material at https://www.scitation.org/doi/suppl/10.1121/10.0015231 for animations of the simulated (SuppPubmm1.mp4) and measured (SuppPubmm2.mp4) cross-correlation sensitivity kernels.

Brooks, L. A., and Gerstoft, P. (**2009**). "Green's function approximation from cross-correlations of 20–100 Hz noise during a tropical storm," J. Acoust. Soc. Am. **125**(2), 723–734.

Brown, M. G., Godin, O. A., Williams, N. J., Zabotin, N. A., Zabotina, L., and Banker, G. J. (**2014**). "Acoustic Green's function extraction from ambient noise in a coastal ocean environment," Geophys. Res. Lett. **41**(15), 5555–5562, https://doi.org/10.1002/2014GL060926.

Brown, M. G., Godin, O. A., Zang, X., Ball, J. S., Zabotin, N. A., Zabotina, L. Y., and Williams, N. J. (**2016**). "Ocean acoustic remote sensing using ambient noise: Results from the Florida Straits," Geophys. J. Int. **206**(1), 574–589.

Buckingham, M. J. (**2011**). "On the two-point cross-correlation function of anisotropic, spatially homogeneous ambient noise in the ocean and its relationship to the green's function," J. Acoust. Soc. Am. **129**(6), 3562–3576.

Carter, G. (**1981**). "Time delay estimation for passive sonar signal processing," IEEE Trans. Acoust, Speech, Signal Process. **29**(3), 463–470.

Cornuelle, B. D., and Skarsoulis, E. K. (**2022**). "Peak-time sensitivity kernels for noise cross-correlation envelopes," J. Acoust. Soc. Am. **151**(4), 2353–2366.

Cron, B. F., and Sherman, C. H. (**1962**). "Spatial-correlation functions for various noise models," J. Acoust. Soc. Am. **34**(11), 1732–1736.

Cron, B. F., and Sherman, C. H. (**1965**). "Addendum: Spatial-correlation functions for various noise models [J. Acoust. Soc. Am. 34, 1732–1736 (1962)]," J. Acoust. Soc. Am. **38**(5), 885.

Douglass, A. S., and Abadi, S. H. "Evaluation of airgun array beam patterns using seismic survey data" (unpublished).

Evers, L., Wapenaar, K., Heaney, K., and Snellen, M. (**2017**). "Deep ocean sound speed characteristics passively derived from the ambient acoustic noise field," Geophysical J. Int. **210**(1), 27–33.

Fried, S. E., Kuperman, W. A., Sabra, K. G., and Roux, P. (**2008**). "Extracting the local Green's function on a horizontal array from ambient ocean noise," J. Acoust. Soc. Am. **124**(4), EL183–EL188.

Godin, O. A. (**2009**). "Accuracy of the deterministic travel time retrieval from cross-correlations of non-diffuse ambient noise," J. Acoust. Soc. Am. **126**(6), EL183–EL189.

Godin, O. A., Brown, M. G., Zabotin, N. A., Zabotina, L. Y., and Williams, N. J. (**2014**). "Passive acoustic measurement of flow velocity in the Straits of Florida," Geosci. Lett. **1**(1), 16.

John Ragland and Shima Abadi

Godin, O. A., Katsnelson, B. G., Qin, J., Brown, M. G., Zabotin, N. A., and Zang, X. (**2017**). "Application of time reversal to passive acoustic remote sensing of the ocean," Acoust. Phys. **63**(3), 309–320.

Langseth, M. G. L. (**2022**). "1905 on research vessel," https://www.rvdata.us/search/cruise/MGL1905 (Last viewed March 1, 2022).

NSF Ocean Observatories Initiative Data Portal (**2022a**). "Low-frequency acoustic receiver [network:OO, station:AXCC1]," https://ooinet.oceanobservatories.org (Last viewed March 1, 2022).

NSF Ocean Observatories Initiative Data Portal (**2022b**). "Low-frequency acoustic receiver [network:OO, station:AXEC2]," https://ooinet.oceanobservatories.org (Last viewed March 1, 2022).

Porter, M. B. (**1992**). "The KRAKEN Normal Mode Program," https://apps.dtic.mil/sti/citations/ADA252409 (Last viewed June 2, 2022).

Ragland, J., Abadi, S., and Sabra, K. (**2022a**). "Long-term noise interferometry analysis in the northeast Pacific Ocean," J. Acoust. Soc. Am. **151**(1), 194–204.

Ragland, J., Schwock, F., Munson, M., and Abadi, S. (**2022b**). "An overview of ambient sound using Ocean Observatories initiative hydrophones," J. Acoust. Soc. Am. **151**(3), 2085–2100.

Roux, P., and Kuperman, W. A. (**2004**). "Extracting coherent wave fronts from acoustic ambient noise in the ocean," J. Acoust. Soc. Am. **116**(4), 1995–2003.

Roux, P., Marandet, C., Nicolas, B., and Kuperman, W. A. (**2013**). "Experimental measurement of the acoustic sensitivity kernel," J. Acoust. Soc. Am. **134**(1), EL38–EL44.

Roux, P., Sabra, K. G., Kuperman, W. A., and Roux, A. (**2005**). "Ambient noise cross correlation in free space: Theoretical approach," J. Acoust. Soc. Am. **117**, 79–84.

Sabra, K. G., Roux, P., and Kuperman, W. A. (**2005**). "Arrival-time structure of the time-averaged ambient noise cross-correlation function in an oceanic waveguide," J. Acoust. Soc. Am. **117**(1), 164–174.

Schwock, F., Ragland, J., Setiawan, L., Munson, M., Volodin, D., and Abadi, S. (**2022**). "OOIPy: A Python toolbox designed to aid scientific analysis Ocean Observatories Initiative (OOI) data," https://doi.org/10.5281/zenodo.4276861.

Siderius, M., and Porter, M. B. (**2008**). "Modeling broadband ocean acoustic transmissions with time-varying sea surfaces," J. Acoust. Soc. Am. **124**(1), 137–150.

Skarsoulis, E. K., and Cornuelle, B. D. (**2019**). "Cross-correlation of shipping noise: Refraction and receiver-motion effects," J. Acoust. Soc. Am. **145**(5), 3003–3010.

Skarsoulis, E. K., and Cornuelle, B. D. (**2020**). "Cross-correlation sensitivity kernels with respect to noise source distribution," J. Acoust. Soc. Am. **147**(1), 1–9.

Snieder, R. (**2004**). "Extracting the Green's function from the correlation of coda waves: A derivation based on stationary phase," Phys. Rev. E **69**(4), 046610.

Tan, T. W., and Godin, O. A. (**2021**). "Passive acoustic characterization of sub-seasonal sound speed variations in a coastal ocean," J. Acoust. Soc. Am. **150**(4), 2717–2737.

Tan, T. W., Godin, O. A., Brown, M. G., and Zabotin, N. A. (**2019**). "Characterizing the seabed in the Straits of Florida by using acoustic noise interferometry and time warping," J. Acoust. Soc. Am. **146**(4), 2321–2334.

Tan, T. W., Godin, O. A., Katsnelson, B. G., and Yarina, M. (**2020**). "Passive geoacoustic inversion in the Mid-Atlantic Bight in the presence of strong water column variability," J. Acoust. Soc. Am. **147**(6), EL453–EL459.

Walker, S. C. (**2012**). "Coherence and interference in diffuse noise: On the information and statistics associated with spatial wave correlations in directional noise fields," J. Acoust. Soc. Am. **131**(3), 1987–1998.

Walker, S. C., and Buckingham, M. J. (**2012**). "Spatial coherence and cross correlation of three-dimensional ambient noise fields in the ocean," J. Acoust. Soc. Am. **131**(2), 1079–1086.

Weaver, R., Froment, B., and Campillo, M. (**2009**). "On the correlation of non-isotropically distributed ballistic scalar diffuse waves," J. Acoust. Soc. Am. **126**(4), 1817–1826.

Weaver, R. L., and Lobkis, O. I. (**2004**). "Diffuse fields in open systems and the emergence of the Green's function (L)," J. Acoust. Soc. Am. **116**(5), 2731–2734.

Woolfe, K., and Sabra, K. (**2015**). "Variability of the coherent arrivals extracted from low-frequency deep-ocean ambient noise correlations," J. Acoust. Soc. Am. **138**, 521–532.

Woolfe, K. F., Lani, S., Sabra, K. G., and Kuperman, W. A. (**2015**). "Monitoring deep-ocean temperatures using acoustic ambient noise," Geophys. Res. Lett. **42**(8), 2878–2884, https://doi.org/10.1002/2015GL063438.

World Meteorological Organization (**2015**). "Manual on Codes - International Codes, Volume I.1: Part A- Alphanumeric Codes" (2015: 2011 edition updated) (Report), p. A-326.

Zang, X., Brown, M. G., and Godin, O. A. (**2015**). "Waveform modeling and inversion of ambient noise cross-correlation functions in a coastal ocean environment," J. Acoust. Soc. Am. **138**(3), 1325–1333.